






Title	Early tsunami detection with near-fault ocean bottom pressure gauge records based on the comparison with seismic data
Author(s)	Mizutani, Ayumu; Yamogida, Kiyoshi; Tanioka, Yuzihiro
Citation	Journal of Geophysical Research: Oceans, 125(9), 2020, JC016275 <a href="https://doi.org/10.1029/2020JC016275">https://doi.org/10.1029/2020JC016275</a>
Issue Date	2020.09
Doc URL	<a href="http://hdl.handle.net/2115/80508">http://hdl.handle.net/2115/80508</a>
Rights	Copyright 2020 American Geophysical Union
Type	article
Additional Information	There are other files related to this item in HUSCAP. Check the above URL.
File Information	Journal of Geophysical Research: Oceans, 125(9), 2020.pdf



[Instructions for use](#)

# Early Tsunami Detection With Near-Fault Ocean-Bottom Pressure Gauge Records Based on the Comparison With Seismic Data

Ayumu Mizutani<sup>1</sup> , Kiyoshi Yomogida<sup>1,2</sup> , and Yuichiro Tanioka<sup>1,3</sup> <sup>1</sup>Department of Natural History Science, Graduate School of Science, Hokkaido University, Sapporo, Japan,<sup>2</sup>Department of Earth and Planetary Science, Faculty of Science, Hokkaido University, Sapporo, Japan, <sup>3</sup>Institute of Seismology and Volcanology, Faculty of Science, Hokkaido University, Sapporo, Japan**Key Points:**

- We propose a new early tsunami detection method with near-fault ocean-bottom pressure gauge records
- The method can be applied to short early records only after 30 s of an origin time
- The resulted waveforms agree well with the tsunami components estimated by a 100-s low-pass filter with sufficiently long records (>500 s)

**Supporting Information:**

- Supporting Information S1

**Correspondence to:**A. Mizutani,  
a\_mizutani@frontier.hokudai.ac.jp**Citation:**Mizutani, A., Yomogida, K., & Tanioka, Y. (2020). Early tsunami detection with near-fault ocean-bottom pressure gauge records based on the comparison with seismic data. *Journal Geophysical Research: Oceans*, 125, e2020JC016275. <https://doi.org/10.1029/2020JC016275>

Received 25 MAR 2020

Accepted 5 AUG 2020

Accepted article online 11 AUG 2020

**Abstract** Offshore real-time ocean bottom networks of seismometers and ocean bottom pressure (OBP) gauges have been recently established such as DONET and S-net around the Japanese islands. One of their purposes is to practice rapid and accurate tsunami forecasting. Near-fault OBP records, however, are always contaminated by nontsunami components such as sea-bottom acceleration change until an earthquake stops its fault or sea-floor motions. This study proposes a new method to separate tsunami and ocean bottom displacement components from coseismic OBP records in a real-time basis. Associated with the Off-Mie earthquake of 2016 April 1, we first compared OBP data with acceleration, velocity, and displacement seismograms recorded by seismometers at common ocean bottom sites in both time and frequency domains. Based on this comparison, we adopted a band-pass filter of 0.05–0.15 Hz to remove ocean-bottom acceleration components from the OBP data. Resulting OBP waveforms agree well with the tsunami components estimated by a 100-s low-pass filter with records of several hundred seconds in length. Our method requires only an early portion of a given OBP record after 30 s of an origin time in order to estimate its tsunami component accurately. Our method enhances early tsunami detections with near-fault OBP data; that is, it will make a tsunami forecasting system faster and more reliable than the previous detection schemes that require data away from source regions or after coseismic motions are over.

**Plain Language Summary** Offshore real-time ocean bottom networks of seismometers and ocean bottom pressure (OBP) gauges have been recently established around the Japanese island. One of their purpose is to realize rapid and accurate tsunami forecasting by near-fault observations. Near-fault OBP records, however, are contaminated by nontsunami components such as sea-bottom acceleration change (i.e., reaction force from the water column above a station), permanent sea-bottom deformation, and ocean acoustic waves or P waves. This study proposes a new real-time method to separate tsunami and sea-bottom displacement components from near-fault OBP records. Our method enables to detect tsunamis accurately with near-fault OBP data only after 30 s of an origin time. Issuing an accurate and rapid tsunami warning with the present method will contribute to significant reduction of tsunami-related casualties.

## 1. Introduction

After the catastrophic disaster caused by large tsunami waves generated by the 2011 Tohoku-oki earthquake, the development of an accurate tsunami early warning system has been an urgent issue in Japan. To improve observation systems for the tsunami early warning, dense cabled observation networks such as Dense Ocean Network system for Earthquake and Tsunamis (DONET Kaneda et al., 2015; Kawaguchi et al., 2015) and Seafloor observation network for earthquakes and tsunami along the Japan Trench (S-net Kanazawa et al., 2016; Mochizuki et al., 2016; Uehira et al., 2016) were newly installed or revised, and they are now operated by the National Research Institute for Earthquake Science and Disaster Resilience (NIED) in the real-time basis. Each station of these networks consists of a seismometer and an ocean bottom pressure (OBP) gauge as multilateral observation. These stations can observe tsunamis directly above fault areas of possible megathrust earthquakes, so they are supposed to provide us with faster tsunami early warnings than ever.

Various tsunami early forecast methods have been recently proposed (e.g., Gica et al., 2008; Jamelot & Reymond, 2015; Wang et al., 2012), and some of them utilize the records of dense seafloor observation networks. For example, Tsunami Forecasting based on Inversion for initial sea Surface Height (tFISH) is a forecast method that estimates the initial sea surface deformation from tsunami waveforms observed at OBP sensors (Tsushima et al., 2012). A tsunami forecast using a large precomputed database, developed by Yamamoto et al. (2016), can rapidly estimate tsunami inundations based on a multi-index method with the comparison of observed tsunami heights and precomputed tsunami heights at OBP gauges. As another type of estimation methods, several data assimilation methods have been developed in which tsunami wave fields can connect OBP data with numerical simulations (Maeda et al., 2015; Tanioka & Gusman, 2018; Wang et al., 2017).

With OBP data, we usually assume the hydrostatic relation between the pressure  $p$  and the tsunami height  $\eta$  above a given site (i.e., sea surface uplift from the reference sea level):

$$p = \rho g \eta, \quad (1)$$

where  $\rho$  is the water density and  $g$  is the gravitational acceleration. Inside a fault area, particularly in a coseismic period, this relation is not satisfied because OBP records change by not only tsunami height but also vertical acceleration of the seafloor (i.e., reaction force from the water column above it), ocean acoustic wave or  $P$  wave radiated from the fault, and permanent sea-bottom deformation due to coseismic fault movement (see Saito & Tsushima, 2016, for details).

Since OBP data are disturbed by these nontsunami components, the estimation of tsunamis inside a fault area is difficult before these motions are terminated, that is, a substantial time delay is required from the origin time. For example, there were substantial nontsunami signals of nearly 5 min in the case of the 2003 Tokachi-oki earthquake ( $M_w$  8.3), as shown later. Rapid separation of tsunami signals from OBP records therefore becomes a key for the above newly developed tsunami-forecast methods to be effective. Warning with less time delay would provide more time for residents along the coast near the epicenter to evacuate.

The main goal of this study is to propose a real-time based method to separate tsunami and sea-bottom displacement components from coseismic OBP data inside a source area. For this purpose, we need to investigate the relationships between OBP data and nontsunami components (i.e., sea-bottom ground motions) at first. In section 3, we shall introduce a correction scheme for ocean-bottom acceleration seismograms to estimate the coseismic waveforms of acceleration, velocity, and displacement. In section 4, we shall compare OBP records with the above sea-bottom ground motions in both time and frequency domains. Time domain analysis is essential because we would like to separate them only with a short-length record for a warning system to work in practice. Based on the results of comparisons, we shall propose our new method to extract tsunami components from coseismic OBP records in section 5. We shall apply our method to OBP data of DONET stations for the 2016 Off-Mie earthquake. Since it was a rather small event, a single record of the 2003 Tokachi-oki earthquake will be also used in order to confirm the applicability to large tsunami events.

## 2. Data

In this study, we analyzed OBP records and strong-motion acceleration records of DONET1 stations (Figure 1). The OBP gauge installed at each DONET station is an absolute quartz oscillation pressure sensor (Paroscientific Inc., model: 8B7000-2). Its properties are as follows: The pressure range is from 0 to 68.96 MPa, and the sampling frequency is 10 Hz (Matsumoto et al., 2013). The properties of each accelerometer (Metrozet, model: TSA-100s) are as follows: The frequency range is from DC to >225 Hz, the sensing range is  $\pm 4$  g, the dynamic range is 135 dB (integrated from 0.1 to 100 Hz), and the sampling frequency is 100 Hz (Japan Agency for Marine–Earth Science and Technology, n.d.; Mary, 2017). To suppress the effect of sea-floor current flows, seismometers are buried in the sea-floor sediment while the OBP gauges are simply sitting on the sea floor.

The event analyzed in this study is the  $M_w$  6.0 Off-Mie earthquake on 2016 April 1 (National Research Institute for Earth Science and Disaster Resilience, 2019) which occurred inside the DONET1 network area (Figure 1). A small scale of tsunamis (<2 cm) was excited and clearly recorded at DONET1 stations (Kubota et al., 2018; Wallace et al., 2016).

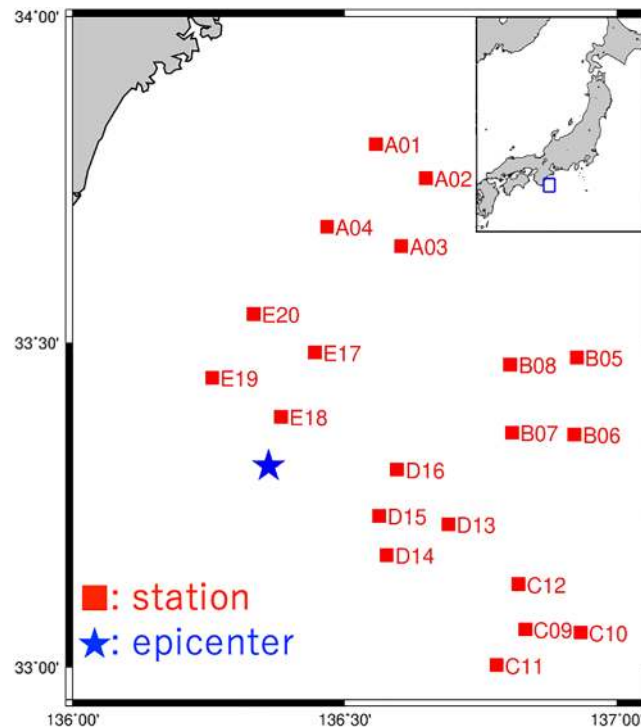


**Figure 1.** Epicenter (blue star) and DONET1 stations (red square) used in this study. The top right panel shows the DONET location in Japan by the blue frame.

As a preliminary data correction, we removed ocean-tide components from original OBP records with a theoretical tide model (Matsumoto et al., 2000). Next, we removed constant offsets by taking the mean of each record in 30 min before the origin time of the earthquake. This offset reflects the installation depth of each station. We shall call the resulting records as “the OBP records” in this study.

Wallace et al. (2016) analyzed OBP records of the same earthquake and determined its coseismic permanent or static displacements. They found the displacement to be 10 cm at station E18, one of the stations close to the epicenter. From the tsunami heights detected at DONET stations, this value should be too large, so they suggested this value to be caused by site rotations due to its strong ground shakings. Nevertheless, we initially attempted to use all the records of the DONET1 stations including E18, because the objective of this study is not to obtain coseismic displacements but to extract tsunami components from the OBP records.

### 3. Data Correction for Strong-Motion Accelerograms

In order to compare near-fault OBP records with vertical ground acceleration, velocity, and displacement seismograms at common sites, any appropriate correction schemes are required. Since the baseline of each acceleration seismogram is not generally fixed in the whole record due to coseismic strong motions, simple integration of an acceleration record for velocity and displacement leads to unreasonable results (e.g., Boore, 2001; Iwan et al., 1985). In this section, we will search for a correction method appropriate for ocean-bottom strong-motion accelerometer seismograms. Note that the resulted acceleration, velocity, and displacement waveforms in this section cannot be used directly for our final goal, tsunami detection method (section 5), but mainly for detail comparisons with OBP records to estimate the characteristics of nontsunami components (section 4). In practice, our proposed correction scheme for strong-motion accelerometer records would take 10 min or more after the earthquake, not suitable for early tsunami warning although it should be useful to check the performance of our method after an earthquake and tsunami waves are over.

The baseline shift of acceleration seismograms has been investigated on land-based strong-motion acceleration data in the long history of earthquake engineering or seismology. For example, Iwan et al. (1985) proposed a scheme that two baselines be removed during and after strong ground motions in record, as shown in Figure 2a. They assumed that strong ground shakings induce a baseline offset ( $a_m$ ) starting at  $t_1$ ,

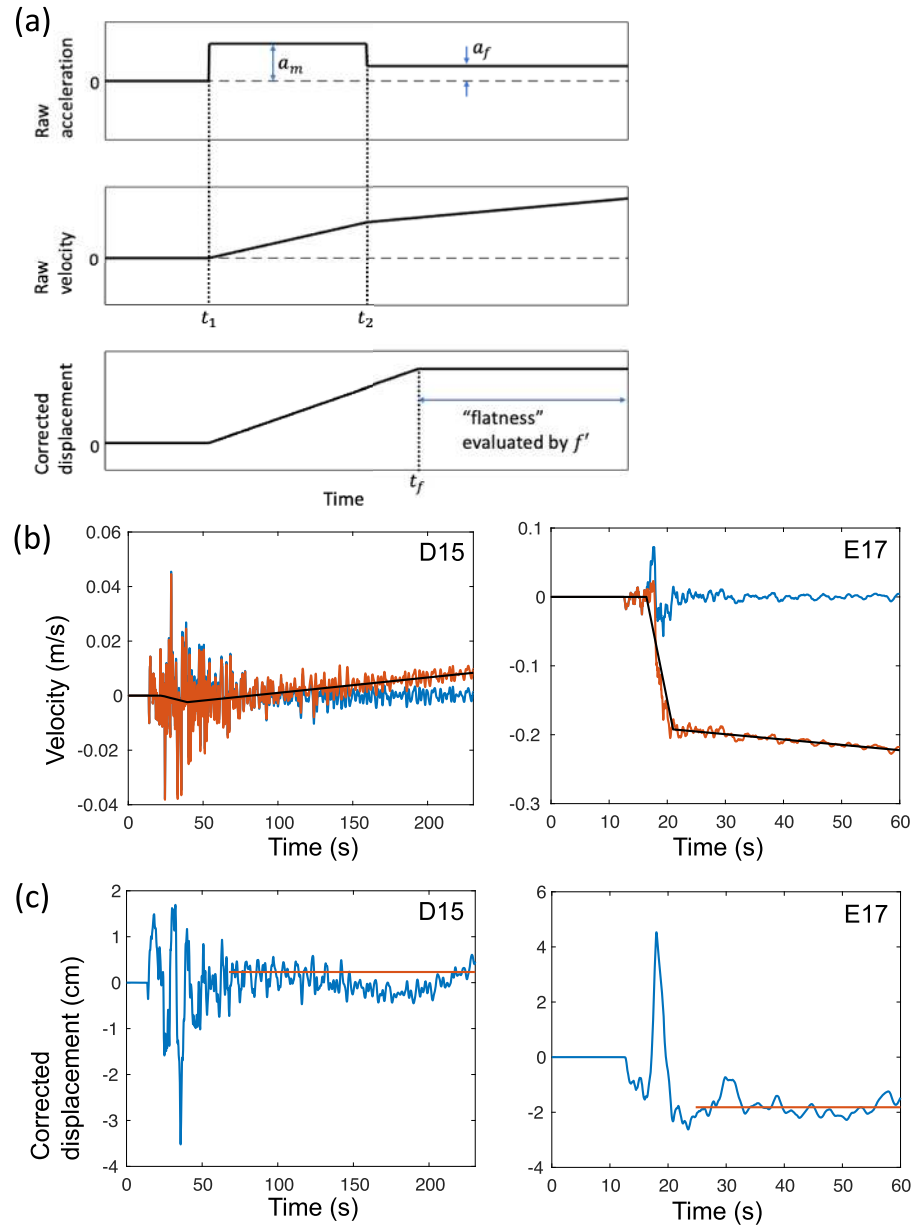


**Figure 2.** (a) Correction scheme for acceleration, velocity, and displacement seismograms. Note that the former two are the waveforms before the correction, while the third is the corrected one. (b) Corrected velocity seismograms (blue lines) and raw velocity seismograms (orange lines) at stations D15 and E17. The black lines represent the trend corrections determined by the method of this study. (c) Corrected displacement seismograms (blue lines) with the residual displacements obtained by OBP records (orange lines) at the two stations.

followed by a residual offset ( $a_f$ ) after the shakings are over at  $t_2$ . These two offsets result in two linear trends for a simply integrated velocity record. Once  $t_1$  and  $t_2$  are determined, using the linear trends in velocity, we can easily estimate  $a_f$  and  $a_m$  by the least squares fit of the velocity record for  $t \geq t_2$ :

$$v_c(t') = v_0 + a_f t', \quad (2)$$

$$a_m = \frac{v_0}{(t_2 - t_1)}, \quad (3)$$

where  $t' = t - t_2$ ,  $v_c(t')$  is the regression line of velocity after  $t_2$ ,  $a_f$ , and  $v_0$  are the slope and the y-intercept of  $v_c(t')$ , respectively. Boore (2001) generalized the method of Iwan et al. (1985) by allowing  $t_1$  and  $t_2$  to be free parameters and showed that various choices of  $t_1$  and  $t_2$  may lead to quite different values for the resulted

residual displacement. A main uncertainty in this baseline correction is, therefore, related to how to choose appropriate values of  $t_1$  and  $t_2$ .

Based on the correction schemes proposed by Iwan et al. (1985), and following the further development of Wu and Wu (2007) and Wang et al. (2011), we developed a new baseline correction method appropriate for DONET strong-motion accelerometer data on the ocean bottom. Similar to the latter two studies, we keep  $t_1$  and  $t_2$  as free parameters and optimize them by a grid search approach in the following ranges:

$$t_{PGA} \leq t_2 \leq t_f, \quad (4)$$

$$t_p \leq t_1 \leq t_2, \quad (5)$$

where  $t_{PGA}$  is the time of the peak ground acceleration (PGA),  $t_f$  is the time roughly estimated for the termination of strong ground shakings, and  $t_p$  is the  $P$ -wave arrival time, respectively. These characteristic times were defined by Wang et al. (2011), so as for the record length  $t_e$  to be used.

The most unique point of the present method is that our goal is to estimate the waveforms of both displacement and velocity, while all of the previous studies focused on the residual or static displacement. In other words, since we are able to estimate a relatively reliable value of residual displacement in the use of an OBP record, we can directly correct the baseline of each accelerogram to match its residual displacement. We introduce  $\Delta d$  as the difference in the residual displacements estimated by OBP and acceleration records. The former is the average from 30 to 50 min after the origin time while the latter follows the correction scheme of Wu and Wu (2007) or the average of the corrected displacement waveform after  $t_f$ . To evaluate the displacement waveform at each iteration in this study, we define a new  $f'$ -value with  $\Delta d$  analogous to the  $f$ -value of Wu and Wu (2007) by

$$f' = \frac{|r|}{|b| \sigma |\Delta d|}. \quad (6)$$

Parameters other than  $\Delta d$  are the same as those of the original  $f$ -value:  $b$  is the slope of the regression line fitted to the corrected displacement waveform from  $t_f$  to the end of the record,  $r$  is the correlation coefficient between the regression line and the corrected displacement waveform, and  $\sigma$  is the variance of the corrected displacement waveform after  $t_f$ , respectively (Figure 2a). If the corrected displacement waveform were perfectly flat,  $|r|$  should be 1,  $b$  should be 0, and  $\sigma$  at its minimum value, that is, the  $f$ -value would reach its maximum. In addition, the smaller  $|\Delta d|$  is, the larger  $f'$ -value becomes, expressing the agreement with the OBP record.

In this study, we applied the new correction scheme of acceleration seismograms with the  $f'$ -value to the records at DONET1 stations for the 2016 Off-Mie earthquake. Wallace et al. (2016) suggested that the residual displacement estimated directly from the OBP record at station E18 of this earthquake should not be reliable, and they concluded that the true residual displacement is  $-4.5$  cm from their fault model. We therefore used this value for the residual displacement of E18, while the displacements at other stations were estimated from their OBP records.

In Figures 2b and 2c, we show two examples of the corrected waveforms at stations D15 and E17. The static displacement observed by each OBP gauge was 0.2 cm and  $-1.8$  cm for D15 and E17, respectively. Then, we found the optimal  $f'$ -value to estimate  $t_1$  and  $t_2$  for the correction of acceleration offset. The residual displacements obtained from the corrected displacement waveforms, which is integrated from corrected acceleration seismograms, are very close to the ones directly measured from their corresponding OBP records. On the other hand, the correction with the  $f$ -value instead of the  $f'$ -value cannot reproduce the residual displacements from the OBP records if the static displacement is not negligible (Figure S1 in the supporting information). We therefore concluded that our correction scheme succeeds in removing the baseline offsets of DONET strong-motion accelerograms recorded on the sea floor.

#### 4. Comparison of Ocean-Bottom Pressure Records and Strong-Motion Seismograms

In this section, we shall compare an OBP record,  $p(t)$ , with the ground acceleration record  $a(t)$  recorded at a common ocean-bottom site, as well as the velocity record  $v(t)$ , and the displacement record  $d(t)$  obtained

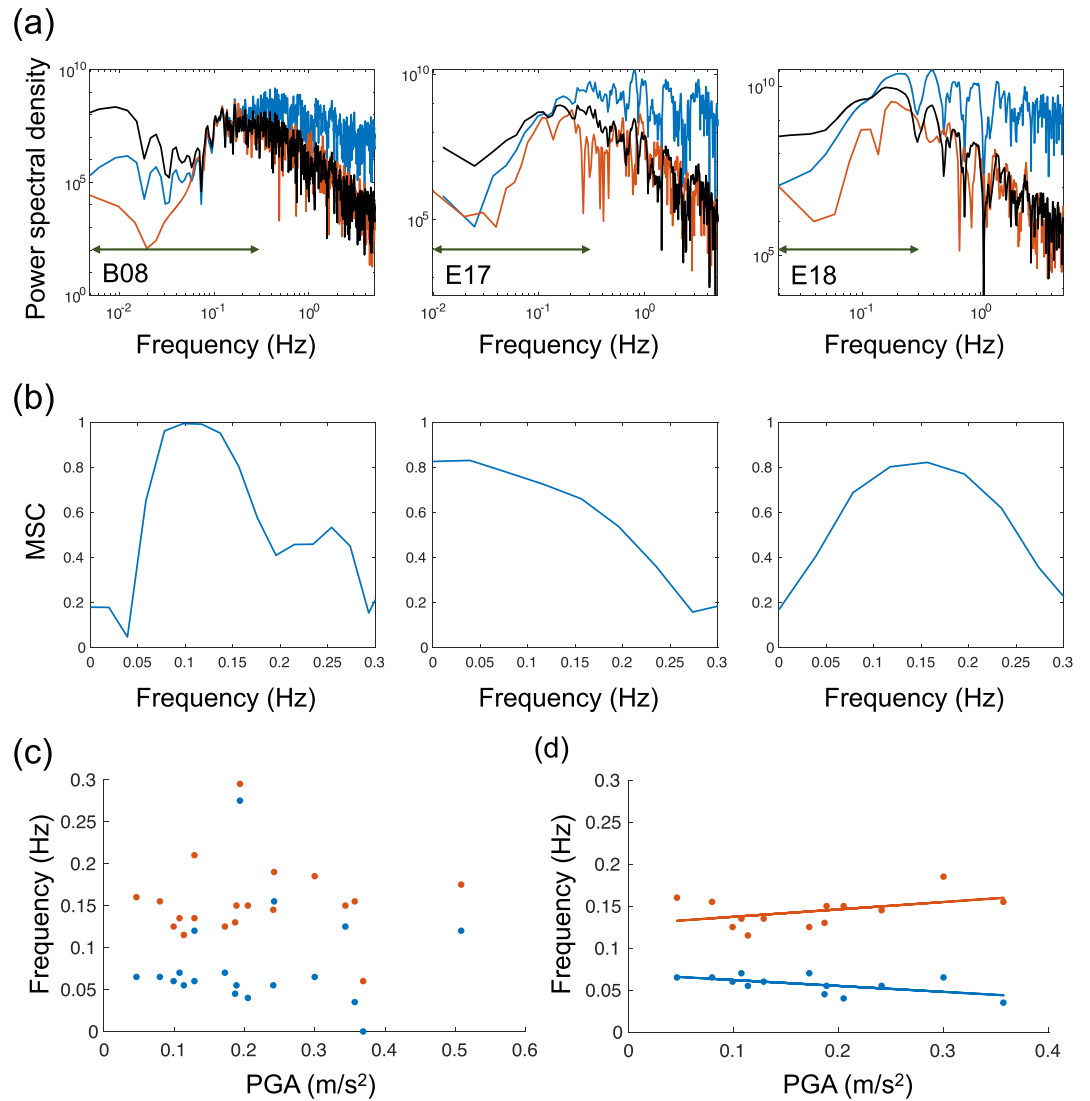


**Figure 3.** (a) Power spectral densities of sea-bottom velocity (black line), sea-bottom acceleration (blue line), and OBP (orange line) records at B08, E17, and E18. B08 is a station far from the fault area, so the amplitudes of their records are much smaller than those at the other two close to it. Each double-headed arrow represents the frequency range of (b). (b) Magnitude squared coherences (MSC) between OBP and sea-bottom acceleration records at B08, E17, and E18. (c) Diagrams of PGA versus lower and upper limits of the frequency range in which OBP data agree with those of sea-bottom accelerations with the threshold of agreement to be  $MSC \geq 0.8$ . Blue and orange dots represent the lower and upper limits at each station, respectively. (d) Same as (c) except that stations A01, A02, A03, D16, E17, E18, and E20 are excluded because the seismograms at these stations may be contaminated by their horizontal components (section 4.2). Blue and orange lines represent the regression lines of the lower and upper limits with correlation coefficients to be 0.57 and 0.42, respectively.

from  $a(t)$  by the method proposed in section 3. We attempt here to clarify the relationship between coseismic OBP changes and sea-bottom ground motions, so we shall set up the basis of the tsunami detection scheme proposed in section 5. We used the following relations to convert the resulted seismograms to their corresponding pressure waveforms (An et al., 2017; Saito, 2017; Saito & Tsushima, 2016):

$$p_a(t) = \rho ha(t), \quad (7)$$

$$p_v(t) = \rho cv(t), \quad (8)$$

$$p_d(t) = -\rho gd(t), \quad (9)$$

where  $\rho$  is the density of sea water,  $h$  is the sea depth of the station,  $c$  is the ocean acoustic wave speed, and  $g$  is the gravitational acceleration. In this study, we adopted the following values:  $\rho = 1030 \text{ kg/m}^3$ ,  $c = 1500 \text{ m/s}$ , and  $g = 10 \text{ m/s}^2$ . Equation 8, for example, represents the pressure  $p_v(t)$  caused by the ocean acoustic wave radiated from the seafloor moving with the velocity  $v(t)$ . Due to the difference in instrumental responses between OBP gauges and acceleration seismometers, we shall investigate in what frequency ranges the above pressure changes are recorded.

#### 4.1. Comparisons in the Frequency Domain

Figure 3a compares power spectral densities of three OBP records and their seismograms corrected in section 3. While OBP spectra agree well with those of sea-bottom acceleration at around 0.1 Hz, they agree with only those of sea-bottom velocity in a higher frequency range, up to 5 Hz. These features are common at most of stations far from the fault area or of small amplitudes. This means that an OBP gauge mainly records sea-bottom ground accelerations at low frequency of around 0.1 Hz but ocean acoustic waves in a wide range of high frequency.

To quantify the relationship between OBP records and sea-bottom accelerations, we applied the cross-spectral analysis using the magnitude squared coherence (MSC) (e.g., Nosov et al., 2018). The MSC is a function of the cross-spectral density, estimated as the Fourier transform of the cross-correlation between two signals. The present MSC takes values from 0 to 1 indicating how well an OBP record is coincident with its corresponding acceleration seismogram at each frequency. Figure 3b shows MSC values at the three stations. As recognized by Figure 3a, OBP indeed agrees with sea-bottom acceleration at around 0.1 Hz at station B08 but not at the other stations. The MSCs between OBP and sea-bottom velocity have also the same characteristics as Figure 3a (Figure S2).

To confirm the above difference among stations whether it is related to the magnitude of ground motions or not, we measured how the frequency range of agreement (i.e., high MSC value) changes with the peak ground acceleration (PGA), commonly used in earthquake engineering. Figures 3c and 3d show the upper and lower limits of the frequency range where MSC exceeds a given threshold. We defined the threshold to be  $\text{MSC} \geq 0.8$ . OBP gauges seem to observe sea-bottom accelerations in the range of 0.05–0.15 Hz, regardless of the PGA value or the magnitude of shakings.

This result is consistent with Matsumoto et al. (2012) who showed an OBP gauge to record sea bottom acceleration in the frequency range between  $f_s = \sqrt{g/4\pi h}$  and  $f_1 = c/4h$ , while ocean bottom velocity at higher than  $f_s$ . On the other hand, this relation cannot be held especially at around 0.1 Hz at E18 and E17, the first and the second closest stations to the epicenter. At these stations, the frequency band that OBP spectra agree with sea-bottom velocity is higher than 0.4 Hz. We shall investigate the cause of this discrepancy as well as how to handle it in section 4.2.

#### 4.2. Comparisons in the Time Domain

The main goal of this study is to evaluate how useful new near-fault OBP records would be in early tsunami detection or warning, so careful comparisons between OBP and seismic records in the time domain should be important with a relatively short record length or only with an early part of each OBP record.

Figure 4a compares the OBP record at B08 with three kinds of its seismic records in the time domain. The amplitude of the pressure waveform is generally similar to that of the velocity waveform, which is also seen at all the stations. We therefore conclude that OBP gauges mainly record ocean acoustic waves during an earthquake. The OBP waveform completely agrees with the velocity waveform particularly at the first several seconds, as shown in Figure 4b on the expanded scale. The time window where the OBP waveform matches the velocity very well corresponds to the round-trip time of the radiated ocean acoustic waves from the sea floor to the sea surface because these durations are clearly correlated with the station depths, as shown in Figure 4c. The ocean acoustic waves reflected at the sea surface are dominant in the OBP record after their perfect match in a few seconds, even after coseismic motions of the sea floor are over. This result with the DONET data agrees well with the numerical simulations of Saito (2017), demonstrating the validity of our baseline correction method for ocean-bottom acceleration records.

Figure 5 compares OBP waveforms with ocean-bottom acceleration records in the time domain with a band-pass filter of 0.05–0.15 Hz whose frequency range was selected from the result of section 4.1. The variance



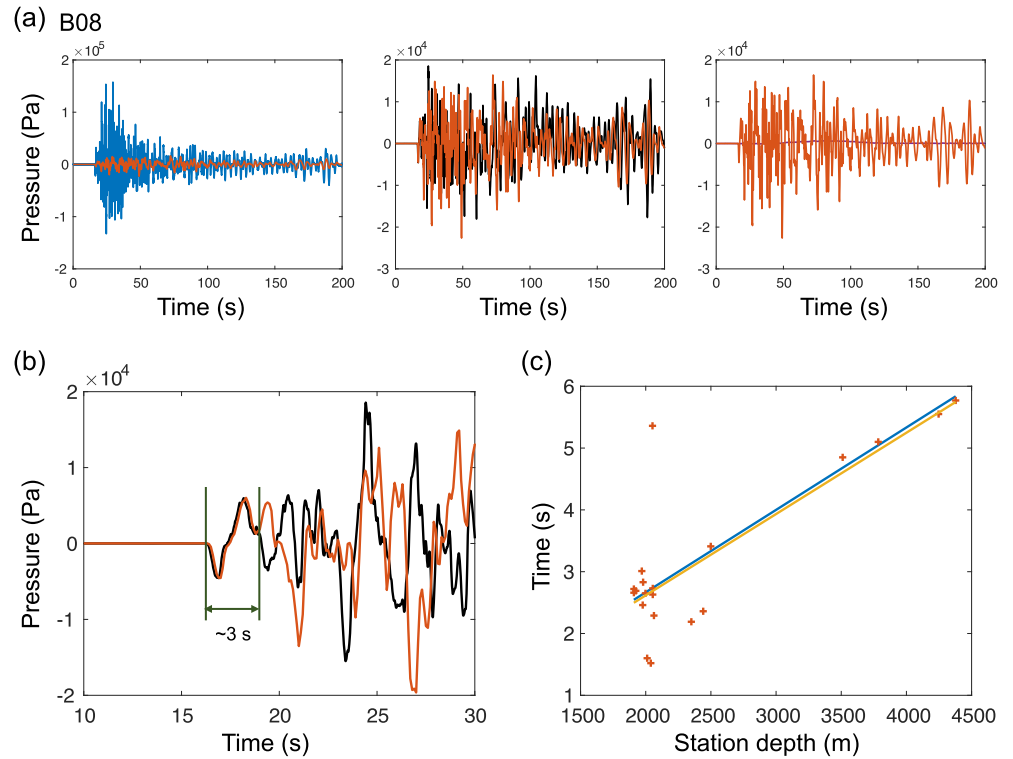


**Figure 4.** (a) Comparisons of the record of OBP (orange) with estimated sea-bottom acceleration (blue, left), velocity (black, center), and displacement (purple, right). Note that the magnitude of plots in velocity and displacement are smaller than that of acceleration, by the factor of 10. (b) Enlarged view of an early part of a comparison of OBP with sea-bottom velocity at station B08. (c) Diagram of the round-trip travel time of ocean acoustic waves between the sea floor and the sea surface (blue line) versus the duration of the OBP waveform that matches its velocity waveform at each station (orange plus sign). The regression line of the data is represented by the yellow line.

reductions (VR) in Figure 5 are often used in the studies with a waveform inversion to evaluate the goodness of waveform fitting between the estimation and observation (e.g., Kubota et al., 2017):

$$VR_{pre-acc} = \left( 1 - \frac{\sum_{k=1}^N (d_k^{pre} - d_k^{acc})^2}{\sum_{k=1}^N (d_k^{pre})^2} \right) \times 100 (\%), \quad (10)$$

where  $N$  is the record length,  $d_k^{pre}$  and  $d_k^{acc}$  are the  $k$ th data points of the band-pass filtered OBP and acceleration waveforms, respectively. While the original acceleration record is quite different from the OBP record, as shown in Figure 4a, the adopted filter yields their good agreement at almost all the stations in Figure 5. The waveforms of six stations A01, A02, A03, D16, E17, E18, and E20, however, show some degrees of discrepancies ( $VR_{pre-acc} \leq 60\%$ ). This may be due to the site conditions of these stations. DONET consists of stations not tightly bolted with the ground beneath them, unlike for stations on land. In addition, OBP gauges and seismometers were not strictly synchronizing their sea-floor motions during an earthquake.

Kubo et al. (2018) suggested that the site amplification effect at the KMA subarray including stations A01, A02, A03, and A04 as well as the KME with E17, E18, E19, and E20 is larger than other stations. Kubo et al. (2019) further suggested that stations A04, B07, B08, D15, D16, E17, E18, E19, and E20 were affected by a certain level of nonlinear soil response during the 2016 Off-Mie earthquake.

Figure 6 shows that the stations at which two waveforms do not agree with each other have relatively large PGA values not only in vertical but also in horizontal components ( $PGA_{horizontal} \geq 2\text{m/s}^2$ ). This result suggests that the disagreements in waveforms at these stations are partly caused by the rotation or tilt of instruments on soft sediment during or after their strong ground shakings.

Let us now discuss the effect of the above disagreement on the tsunami detection scheme to be proposed in this study. In Figures 5 and 6, the agreement of the waveforms at D14 is rather good, even though the vertical PGA value is as large as, for example, A01, a disagreement station. In contrast, the horizontal PGA at D14 is

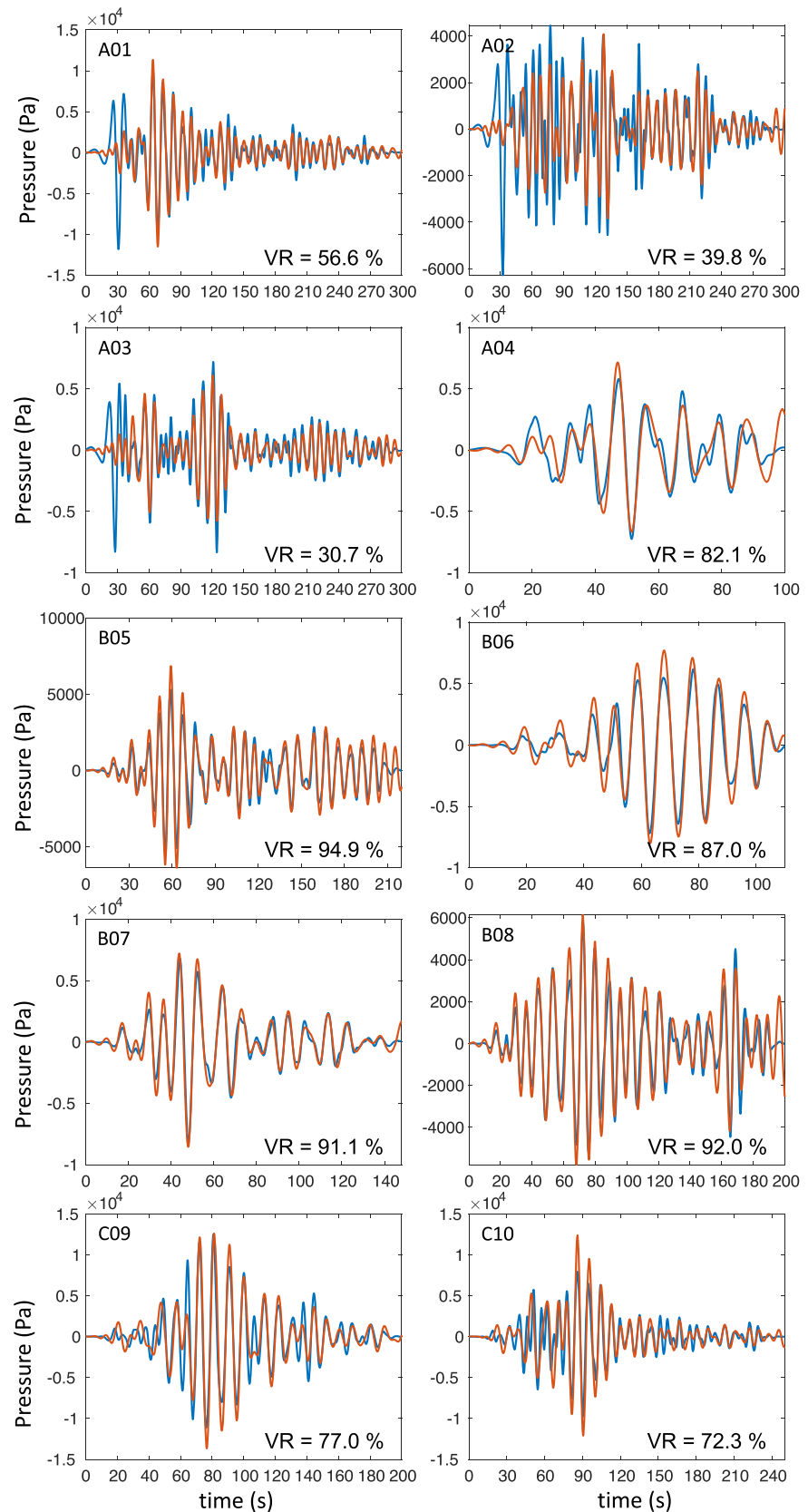


**Figure 5.** Comparisons of OBP (orange line) and sea-bottom vertical acceleration (blue line) records with a band-pass filter of 0.05–0.15 Hz at all the stations. We define the variance reduction (VR) by Equation 10.

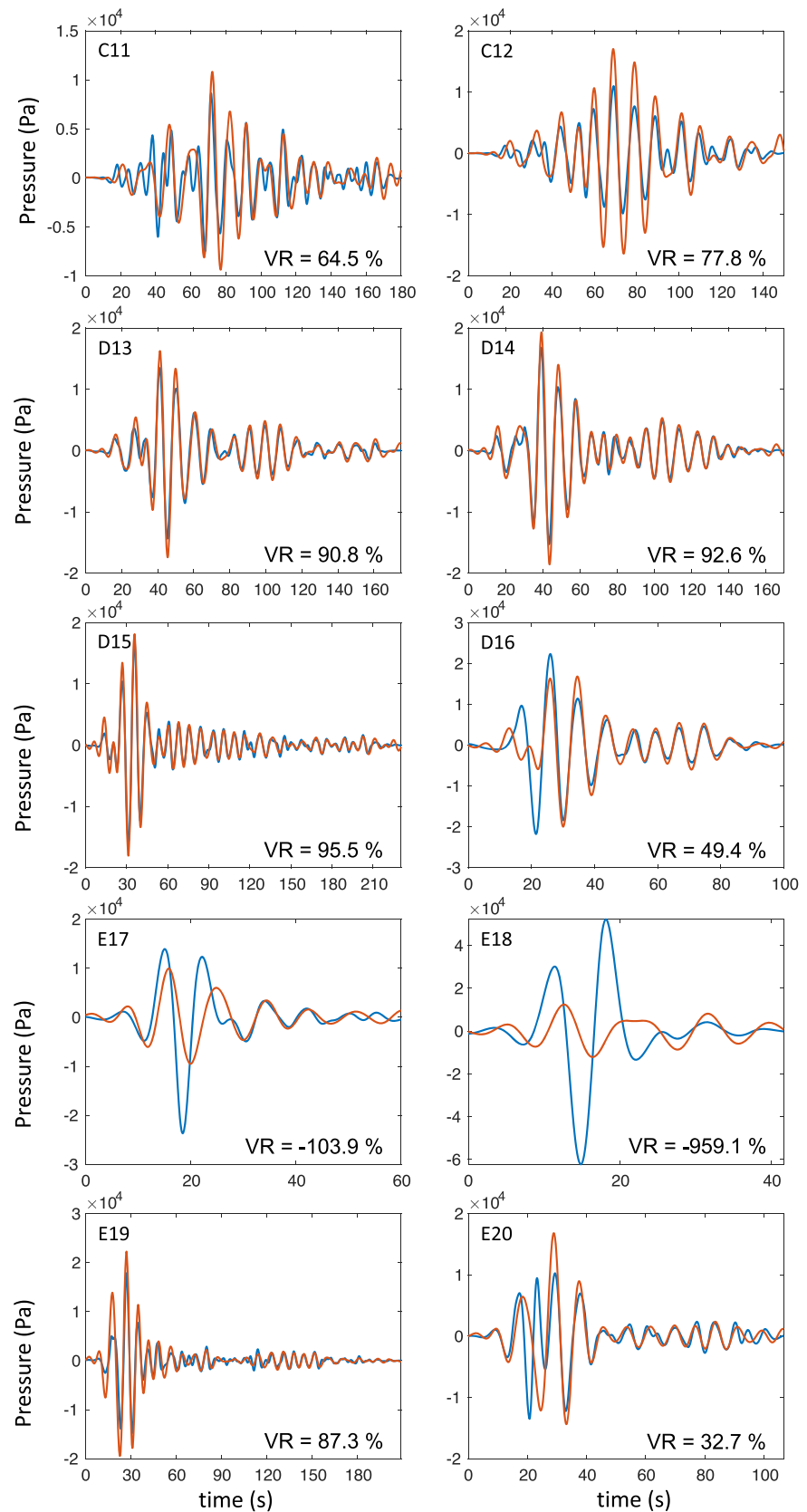
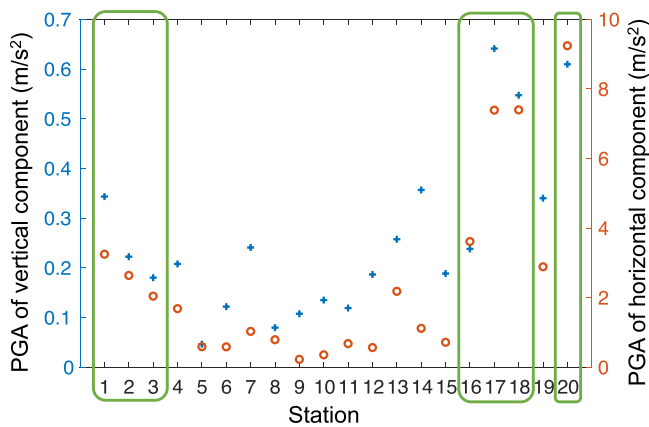


Figure 5. (Continued)



**Figure 6.** Peak ground accelerations (PGA) of vertical (blue plus sign) and horizontal (orange circle sign) components at each station. Green squares represent stations whose variance reduction in Figure 5 is less than 60%. The horizontal is defined by the square root of the sum of squares of two horizontal components.

smaller than A01. We can find such a feature at other stations, so the above disagreement is probably caused by large ground shakings of not vertical but horizontal components. To confirm this cause, we compared the band-pass filtered waveforms of 0.05–0.15 Hz with the accelerations of horizontal components at the stations of low VR or disagreement in Figure 7. Most of the disagreements in waveforms can be found only during strong motions in the horizontal components, where vertical acceleration waveforms are also large but not so large in OBP records. It may be natural that strong horizontal ground motions affect vertical acceleration seismograms because ocean-bottom seismometers of DONET are not tightly locked with the sea floor. The disagreements between OBP and vertical seismic records at same stations are concluded due to vertical accelerations induced by strong horizontal ground motions. In other words, OBP gauges of DONET may punctually record sea-bottom accelerations at around 0.1 Hz, regardless of the magnitude of ground motions at least associated with the present earthquake.

Stations A01, A02, A03, D16, E17, E18, and E20 are excluded in Figure 3d for the above reason (i.e., large horizontal shakings). Unlike the result with all the stations (Figure 3c), we can clearly recognize that OBP gauges indeed record sea-bottom accelerations well in the frequency range of 0.05–0.15 Hz.

We can therefore conclude that the records of DONET OBP gauges seem to agree with sea-bottom accelerations at 0.05–0.15 Hz even with relatively large shakings and their severe site condition sitting on soft sediment of the sea bottom.

## 5. Application to Early Detection of Tsunamis

### 5.1. Proposed New Scheme

Having confirmed the relationship between coseismic OBP records and ground motion seismograms in section 4, we now propose a new scheme for tsunami early detection with ocean bottom networks such as DONET. That is, we attempt to extract tsunami and sea-bottom displacement components only from an early part of OBP data. Note that our new tsunami detection scheme essentially uses only OBP data because the calculation of displacement waveforms from acceleration seismograms generally takes a long time as explained in section 3. Considering the results of our analyses with DONET data, we can assume that any OBP gauge records sea-bottom accelerations accurately at least in the frequency range of 0.05–0.15 Hz. We shall therefore need to remove the accelerations from each OBP record with an appropriate band-pass filtering.

Our new early detection scheme of tsunamis is therefore realized by the following steps, as shown in Figure 8a:

1. Extract a series of short records of OBP with the 60-s time window (20% of the Tukey window) shifted by the 10-s interval.
2. Apply a low-pass filter of 0.15 Hz to each of the above 60-s records (Step 1) to make a record including tsunami, displacement, and acceleration components (i.e., to remove velocity component). As shown in section 4, velocity components mainly exist at higher than 0.15 Hz.
3. Apply a band-pass filter of 0.05–0.15 Hz to the original 60-s records (Step 1) to make a record including only acceleration components.
4. Subtract the band-pass filtered waveform (Step 3) from the low-pass filtered waveform (Step 2) to remove the acceleration components.

The resulted waveform should mainly consist only of tsunami and displacement components because we are supposed to remove velocity components in Step 2 and remove acceleration components in this step.

5. For each of the waveforms of Step 4, we take the average from 6 to 54 s or discard both ends of the waveform in time because we have used a 20% Tukey window to make 60-s records at Step 1.

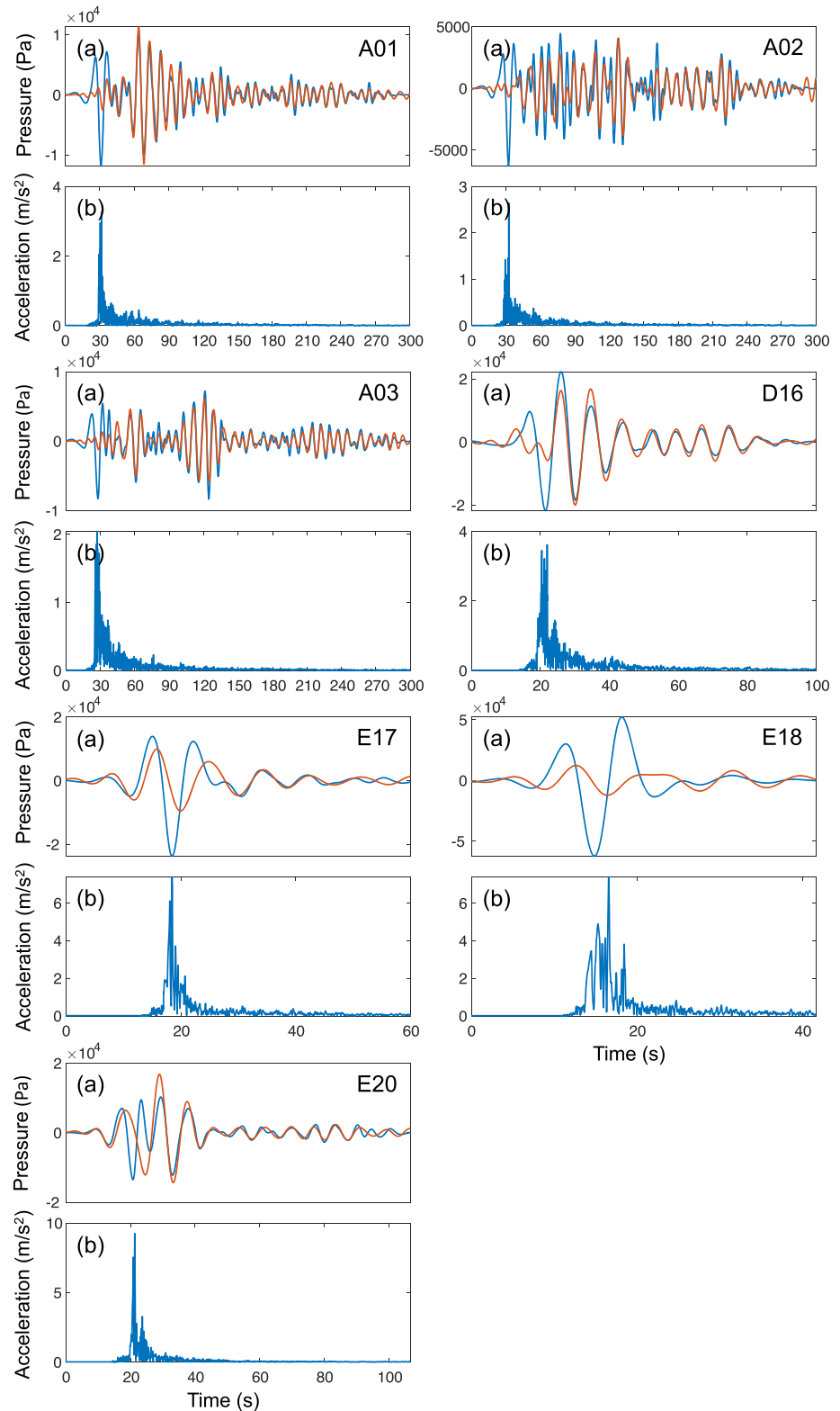


**Figure 7.** Time-domain comparisons between (a) the band-pass filtered waveforms of 0.05–0.15 Hz and (b) horizontal accelerations at stations A01, A02, A03, D16, E17, E18, and E20. The band-pass filtered waveforms are same as those in Figure 5. The horizontal at each station is defined by the square root of the sum of squares of its two horizontal components.

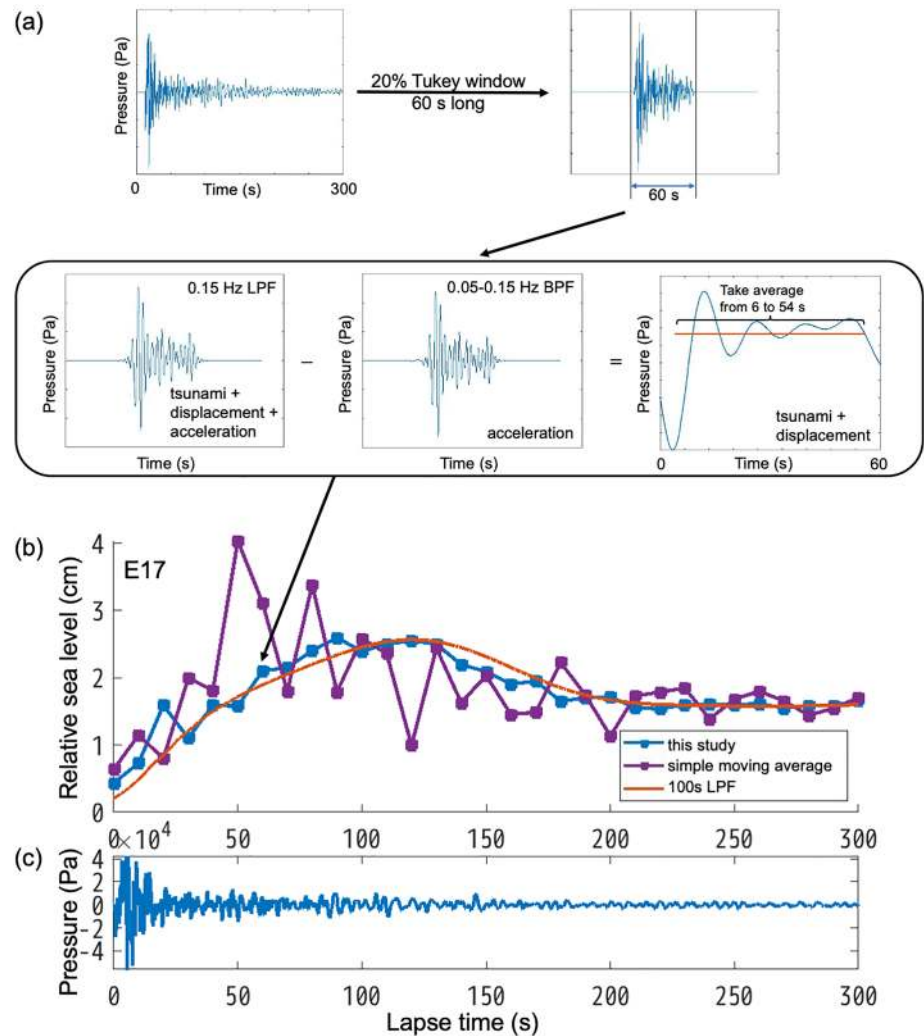


**Figure 8.** (a) Schematic diagram of the tsunami early detection scheme proposed by this study. The orange line in the waveform in the center right represents the average from 6 to 54 s of one of the 60-s waveforms, which should correspond to signals of tsunami and displacement. (b) Comparison of the result of the method of this study (blue line), the 60-s moving average (purple line), and the 100-s low-pass filtered waveform (orange line) at station E17. Each dot represents an estimated value at 10-s intervals. Note that there is a tsunami signal at 50 to 200 s of this record. (c) Its original OBP record after tide and station depth components are removed.

Each of 60-s waveforms yields one value (the average), with which we make the final waveform for possible tsunami and displacement signals with the original record length of Step 1.

In each of Steps 2 and 3, we applied a second-order Butterworth filter to OBP records both forward and backward in time. The length of the time window in Step 1 (60 s) is determined by the restriction from the low cut-off frequency of the band-pass filter in Step 3. We applied the band-pass filter of 0.05–0.15 Hz or 6–20 s in period, so the length of our time window becomes three times of 20 s.

This scheme, particularly in Step 5, is similar to a kind of data smoothings by the moving average of a given waveform. In the moving average method, the average value for the 60-s time window at a given time is taken from 30-s data on both sides of that time. We can therefore obtain our final waveform, considering it as tsunami and displacement signals, only after 30 s of the origin time or the starting time of shakings at each station.

## 5.2. Application to the Off-Mie Earthquake

We applied the above proposed scheme to the OBP data at near-fault DONET1 stations of strong coseismic shakings associated with the 2006 Off-Mie earthquake. Figure 8b shows the final waveform of station E17

processed by the present scheme, compared with the waveforms with a 100-s low-pass filter applied to the original record of 5400 s in length as well as with its simple moving average. The low-pass filtered waveform with a long record is a kind of conventional approaches to retrieve tsunami signals from OBP data as well as traditional tsunami data such as a tidal gauge at the ocean coast. The output of our new scheme clearly agrees with the 100-s low-pass filtered record much better than the simple moving average of the original OBP record, especially in the first 100 s. We can recognize a signal of tsunamis at 50 to 200 s of the waveform obtained by the 100-s low-pass filter together with our method. It is natural that the result of our method is relatively similar to that of the moving average after 150 s where the effect of strong shakings become negligible (Figure 8c). In other words, our method successfully removes the acceleration and velocity components of sea-floor motions that masks the tsunami signal in the original OBP record, particularly in its early part.

Figure 9 shows the results at all the stations, including those with relatively weak shakings even in their coseismic periods. We can identify clear tsunami signals at 50 s (station E18), at 150 s (E17, E19, and E20), at 200 s (D15 and D16), at 250 s (D13 and D14), and at 280 s (A04 and B07), respectively. At other stations (i.e., A01, A02, A03, B05, B06, B08, C09, C10, C11, and C12), tsunami signals are rather weak because these stations are far from the epicenter (Figure 1), and tsunamis did not arrive in 300 s. Because of their long epicentral distances, the signals of tsunami and acceleration at these stations are separated in their time-domain records, so any traditional low-pass filtering methods may work well with these data.

Note that, however, tsunami warnings which use only the records of these stations must wait much longer than the present scheme. For example, considering that a standard tsunami inversion technique requires at least a quarter of the waves in record, the records with our method at 10 near-fault stations (A04, B07, C13, C14, C15, C16, E17, E18, E19, and E20) seem to be sufficient within 300 s after the origin time in this case.

Figure 10a shows standard errors of the present method versus the simple moving average, relative to the 100-s low-pass filtered records for all the stations as a function of lapse time. While our signals retrieved from the OBP records of a short record length agree well with the low-passed waveforms of a long record length, the waveforms with the simple moving average show large discrepancies from possible tsunami signals. The maximum of the standard errors of our method (50 Pa) is about half of that of the simple moving average (110 Pa), and it is also much less than the tsunami amplitude of this event (2 cm or 200 Pa).

The disagreement of the simple moving average is significant particularly at stations close to the fault area or those with large shakings and tsunami signals (Figure 9). That is, our approach should be effective for the purpose of reliable tsunami detection in the use of real-time near-fault OBP data.

### 5.3. Application to the 2003 Tokachi-oki Earthquake

In the development of the extraction method of tsunamis from near-fault OBP records and strong-motion data at common sites, we used the DONET data of the 2016 Off-Mie earthquake. Since it was a small event ( $M_w$  6.0) with very weak tsunamis (<2 cm), all the adopted parameters of the method may not be applicable to other events, particularly to earthquakes that excite much larger tsunamis for its practical use of early tsunami warning. At present, however, OBP networks have just started their operations. Fortunately, there were a few OBP records available around Japan before the installation of DONET and S-net stations. One of them is the OBP records near the  $M_w$  8.3 Tokachi-oki earthquake on 2003 September 26. It had been the largest recent subduction-zone megathrust earthquake around Japan until the 2011 Tohoku-oki earthquake (e.g., Honda et al., 2004; Yamanaka & Kikuchi, 2003), and substantial tsunamis of the maximum of 4 m run-up height were observed along the coast of the southeast Hokkaido Island (Tanioka et al., 2004).

OBP gauges (PG1 and PG2) were installed as a cabled ocean-bottom observation system by the Japan Agency for Marine-Earth Science and Technology (JAMSTEC) (Hirata et al., 2002), and tsunami waves were clearly recorded. In addition to the OBP stations, seismic stations (OBS1, OBS2, and OBS3) were also installed in this ocean-bottom area. Since station OBS1 was located close to the station PG1 (5 km apart), we may consider it to be the same site of the OBP data, as in the case of DONET (Figure 11a). The vertical PGA of OBS1 was  $1.54 \text{ m/s}^2$ , about three to four times larger than the DONET data used in the previous section.

We followed the same procedure with the OBP data of PG1 as the DONET data, that is, removing the ocean-tide and installation depth components at first, followed by extracting tsunami and displacement components, as explained in section 5.1.

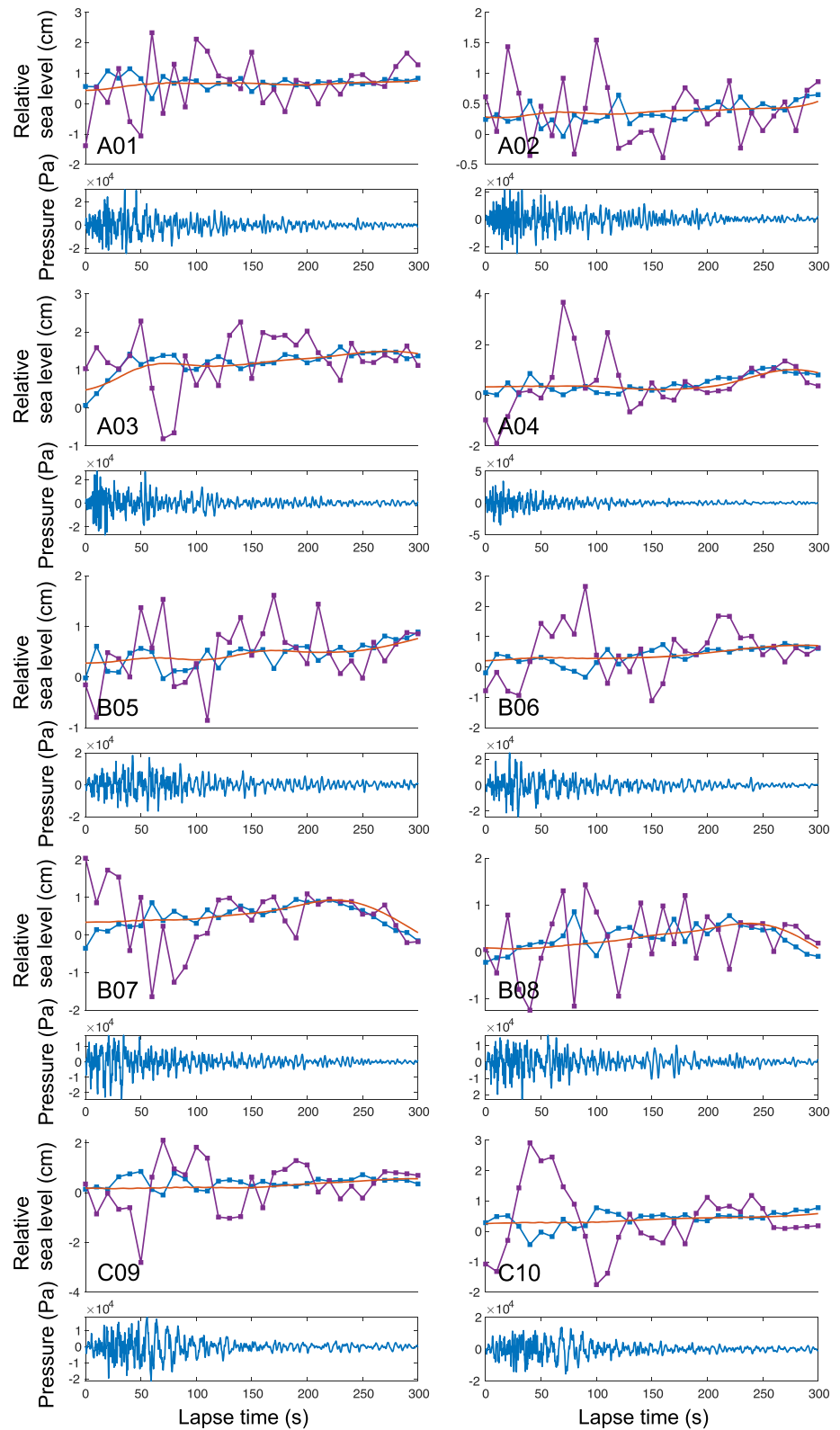


Figure 9. Same as Figures 8b and 8c except for all the stations.



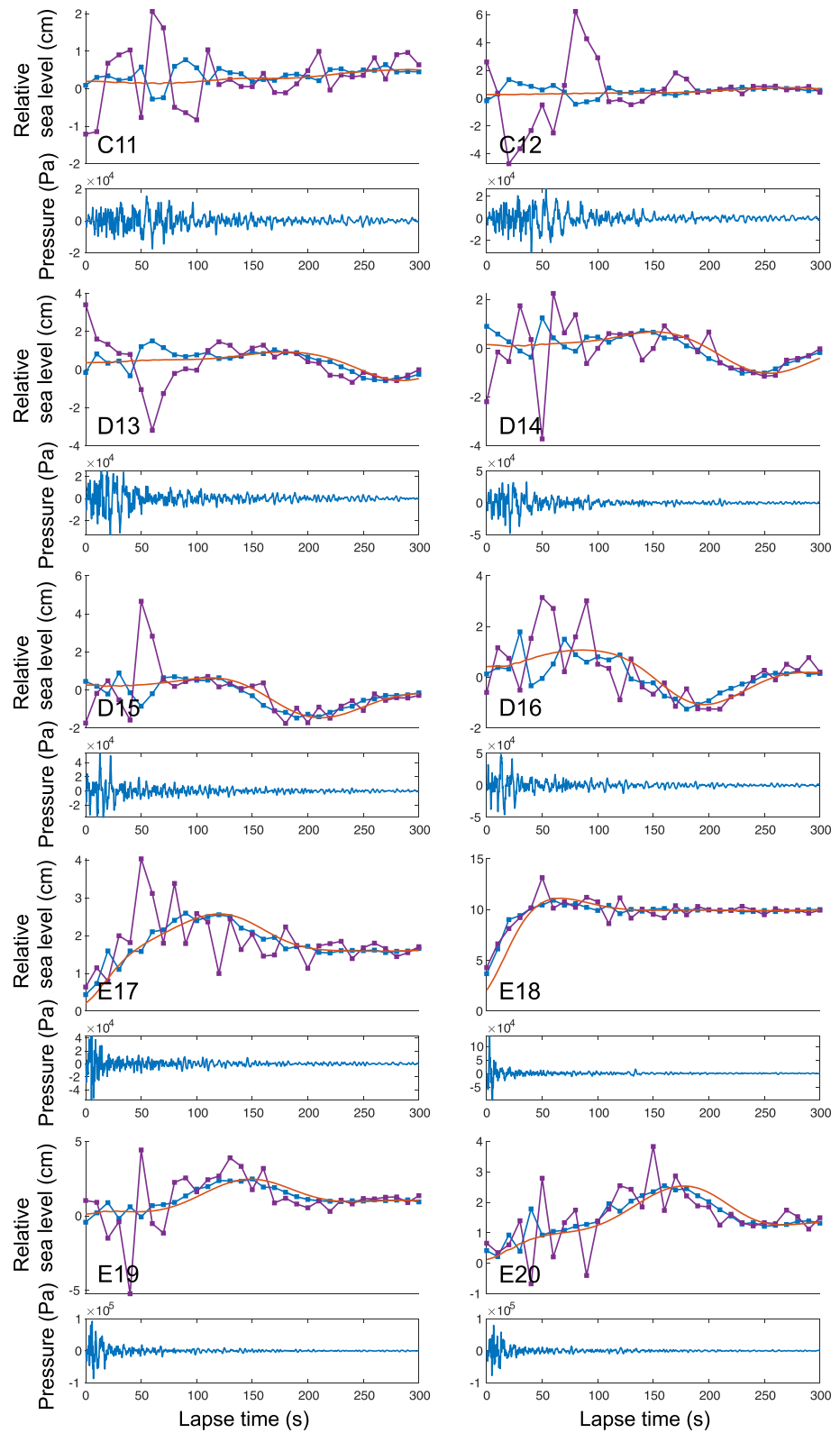
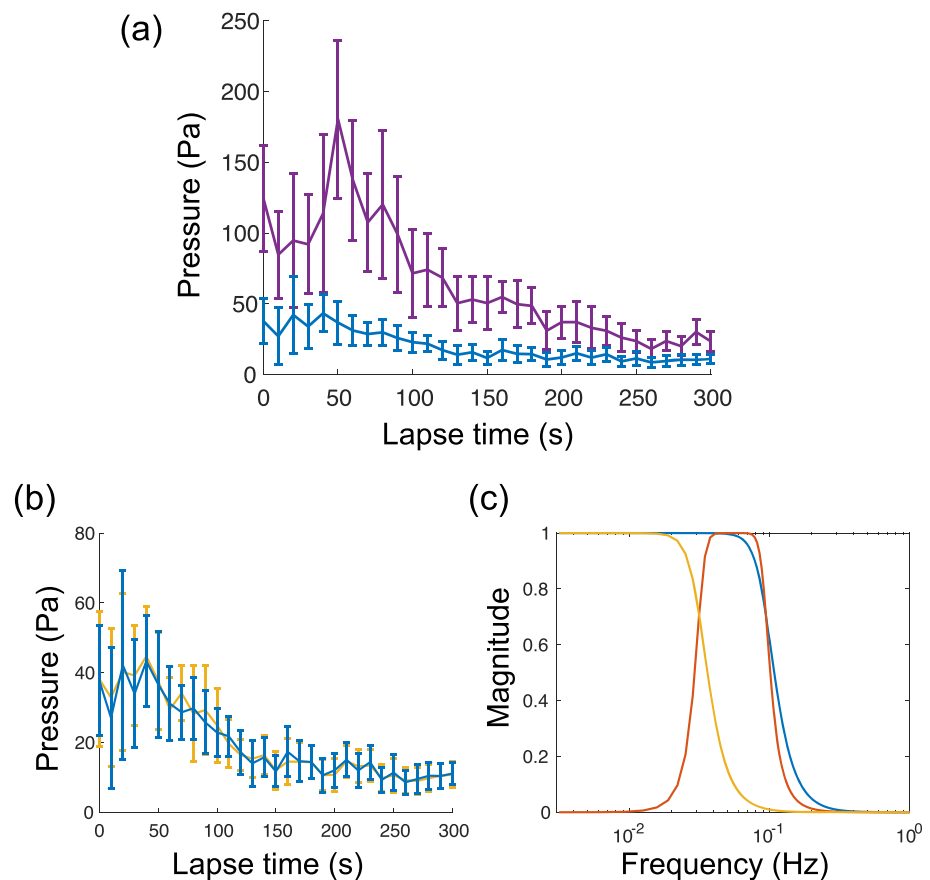


Figure 9. (Continued)



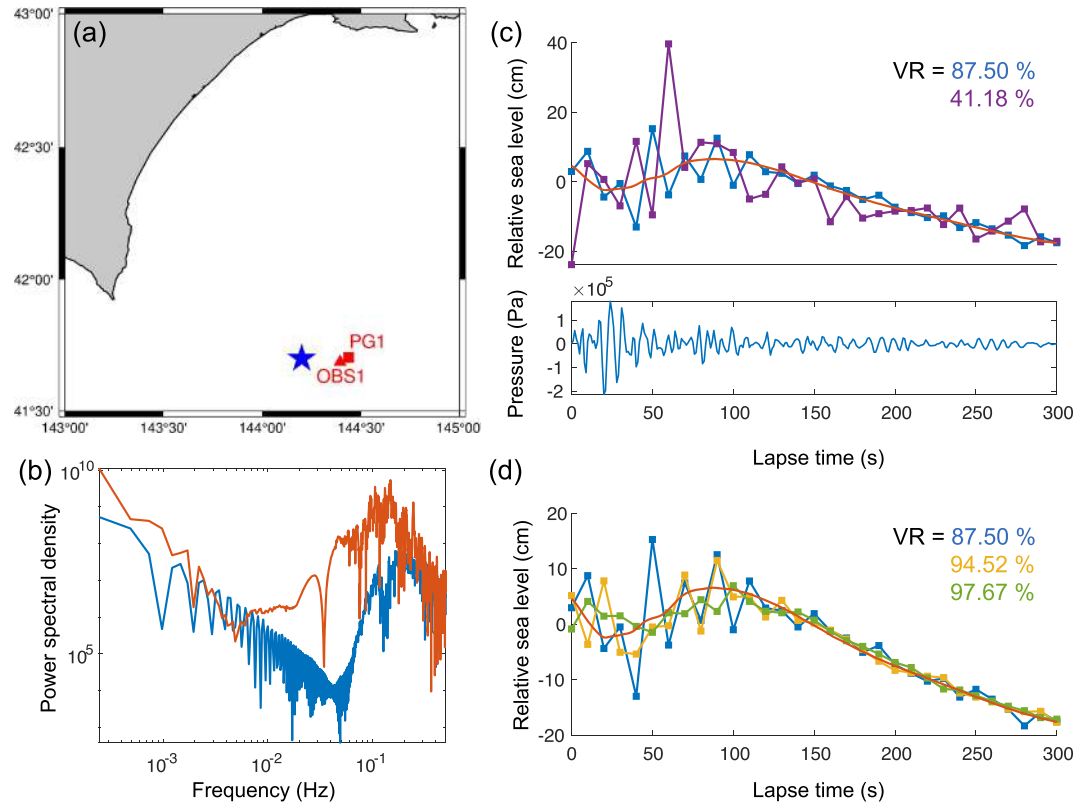
**Figure 10.** (a) Means and standard errors of difference from the 100-s low-pass filtered records at all the stations as functions of lapse time. The blue line represents the waveforms obtained by this study, while the purple line is for 60-s moving averages. Note that the amplitude of tsunami is about 2 cm or 200 Pa. (b) Same as (a) except that the yellow line represents the results of applying only a single low-pass filter of 0.05 Hz instead of a band-pass filter of 0.05–0.15 Hz in Steps 3–4. The blue line represents our approach same as (a). (c) Frequency responses of fourth-order Butterworth filters. The blue, orange, and yellow lines represent the low-pass filter of 0.15 Hz, the band-pass filter of 0.05–0.15 Hz, and the low-pass filter of 0.05 Hz, respectively.

Figure 11b compares power spectral densities (PSD) between the 2016 Off-Mie earthquake (E18 of DONET1) and the 2003 Tokachi-oki earthquake (PG1). The amplitude of PSD of PG1 is larger than E18 at almost all the frequency by the factor of 10–100. The PSD peak of PG1 is shifted to lower frequency: about 0.1 Hz for PG1 versus 0.2 Hz for E18. These differences reflect their size, differing by 1,000 times in seismic moment.

Figure 11c show the result of the present scheme to the OBP data of PG1, using the same parameters as the DONET1 case shown in Figures 8b and 9. Despite the significant difference of their spectra both in size and dominant frequency, our result successfully expressed tsunami components (i.e., low-pass filtered of 100 s) extracted from the original OBP data than the simple moving average, even with the parameters estimated by the small Off-Mie earthquake.

The main period of tsunami signals is longer than 100 s for either small or large, while the dominant frequency range of strong ground shakings is covered mostly by the adopted parameters of the filters in the present method (section 5.1). As a result, the retrieval scheme proposed in this study may become effective for the practical tsunami warning even with large events or tsunamis such as the 2003 Tokachi-oki earthquake.

Note that the gentle decrease after 100 s in Figure 11c is due to the propagation of tsunamis but not ground shakings. The similar character can be observed inside the source region, and the decrease continued up to 20 min after the origin time in the case of this earthquake (Tsushima et al., 2012). We cannot identify such



**Figure 11.** (a) Locations of the epicenter (blue star), an ocean bottom pressure gauge (red square), and an ocean bottom seismometer (red triangle) used for the 2003 Tokachi-oki earthquake. (b) Power spectral densities of E18 for the 2016 Off-Mie earthquake (blue line) and PG1 for the 2003 Tokachi-oki earthquake (orange line). Note that the frequency range is wider than Figure 3a. (c) Same as Figures 8b and 8c except for PG1 for the Tokachi-oki earthquake. The variance reductions (VR) defined by Equation 11 are represented by the same colors. (d) Same as (c) except that the results are obtained by three types of band-pass filters. Blue, yellow, and green lines represent the results by the band-pass filters of 0.05–0.15 Hz, 0.04–0.15 Hz, and 0.03–0.15 Hz, respectively. The waveform of the blue line is the same as (c).

waveforms at DONET stations (Figure 9) because the source area of the 2016 Off-Mie earthquake is much smaller than that of the 2003 Tokachi-oki earthquake, resulting a shorter dominant wavelength of tsunamis.

Since we analyzed the single record of PG1, we cannot make any statistical evaluations such as the standard error analysis conducted in section 5.2 or Figure 10a. We therefore defined another kind of variance reductions to evaluate the agreement with the 100-s low-pass filtered waveform analogous to Equation 10 in this case:

$$VR_{LPF-EX} = \left( 1 - \frac{\sum_{k=1}^N (d_k^{LPF} - d_k^{EX})^2}{\sum_{k=1}^N (d_k^{LPF})^2} \right) \times 100 (\%), \quad (11)$$

where  $d_k^{LPF}$  and  $d_k^{EX}$  are the  $k$ th data points of the waveforms obtained by the 100-s low-pass filter and the adopted extraction method (i.e., our method or the simple moving average), respectively.

The variance reductions of our method and the simple moving average are 87.50% and 41.18%, respectively (Figure 11c). In other words, our method can also provide much better results than the simple moving average even for large  $M8$ -class earthquakes.

#### 5.4. Discussion

In this section, we discuss each step of our extraction method and its practical applicability to possible megathrust earthquakes in detail.

Because original OBP gauges give the absolute pressure values, this study preliminarily removed constant offsets by taking the mean of each OBP records in 30 min before an earthquake (section 2). For the practical operations of our extraction method, this preliminary correction may be easily done because the OBP gauges of DONET or S-net observe OBP changes in real time. Specifically, as same as an earthquake is detected at the closest station, the average of each OBP record is calculated and removed at other stations even before their changes start.

In early steps, we need to apply two filters (i.e., the low-pass filter of 0.15 Hz and the band-pass filter of 0.05–0.15 Hz), followed by the subtraction of the band-pass filtered waveform from the low-passed one. It appears to be similar to applying low-pass filter of 0.05 Hz directly to the 60-s OBP records. Figure 10b compares the result of our scheme with that of the possible single low-pass filtering process, clearly proving that our fine-tuned multistep filtering process yields small errors in result than the single filtering process particularly in early parts of strong shakings. This difference is due to the passband characteristics of the filters (Figure 10c). In other words, a careful filter setting of band pass characteristics is required, so the careful comparison of OBP and strong motion data in section 4 is extremely effective.

In Figure 9, we can see a large offset (1,000 Pa or 10 cm) at station E18. This offset is due to displacement component of its strong shakings, as pointed out by Wallace et al. (2016). Our method, however, provides good agreement with the 100-s low-pass filtered waveform, that is, the tsunami component is correctly estimated even at stations of such unstable conditions. Since unreliable displacement components may cause some errors in tsunami source estimation (e.g., Kubota et al., 2018; Wallace et al., 2016), estimating the amount of sea-bottom displacement precisely should be an important ongoing research theme. Although technical improvements such as arrangement of good installation environment will be achieved in the future, the development of efficient and stable analytical methods will be also essential.

The most important assumption of our method is that OBP gauges observe sea-bottom acceleration in the frequency range of 0.05–0.15 Hz from the comparison between the records of OBP gauges and accelerometers in section 4. Though the magnitude of the earthquake in this study was  $M_w$ 6.0, we can obtain a good result at least for a single OBP record of the  $M_w$ 8.3 Tokachi-oki earthquake with the same assumption (Figure 11c).

On the other hand, because of the small slope of the regression lines in Figure 3d, the frequency range where accelerations are contaminated in OBP records may increase in proportion to the PGA value or the size of earthquakes. To confirm this effect, we compared three types of band-pass filters in Step 3 to the OBP data of the Tokachi-oki earthquake: 0.05–0.15 Hz, 0.04–0.15 Hz, and 0.03–0.15 Hz (Figure 11d). Since we apply the low-pass filter of 0.15 Hz in Step 2, the highest frequencies of these band-pass filters should not affect the results. Note that the lengths of time windows had to be changed for 60, 75, and 100 s, respectively, because each record length needs to be three times of the low cut-off frequency of each band-pass filter, as explained in section 5.1. The stating time of our estimation is also changed to be 30, 37.5, and 50 s after the earthquake, respectively.

Figure 11d shows the results with variance reductions of the resulted waveforms defined by Equation 11. The wider a band-pass filter is, the larger the variance reduction becomes, as naturally recognized. Each variance reduction is 87.50%, 94.52%, and 97.67% for the bands of 0.05–0.15 Hz, 0.04–0.15 Hz, and 0.03–0.15 Hz, respectively. There is clear improvement from the first to the second filters. We therefore conclude that the cut-off frequency of accelerations appropriate to large earthquakes is about 0.04 Hz. This leads to slight delay for our first estimation time, although less than 10 s.

Note that, however, the variance reduction of the highest (0.05–0.15 Hz) band-pass filtered waveform is rather satisfactory. A high frequency filter requires only a short piece of records, and the longer the length of time window, the slower the estimation of tsunami and displacement components. In other words, there is a trade-off between the accuracy and the immediacy of estimations. We propose the use of the 0.05–0.15 Hz filter in this study, appropriate for tsunami early warnings, not only for small earthquakes but also for large ones.

The duration time of strong shakings becomes large with the increase of the size of earthquakes. Since our method extract tsunami signals from an early part of OBP records contaminated by other signals such as ground shakings, it should be more powerful with large events of longer duration in shakings.

## 6. Conclusions

In order to develop a new early tsunami detection method, we analyzed the records of OBP gauges and ocean bottom accelerometers of DONET1 associated with the Off-Mie earthquake of 2016 April 1 which occurred inside its network area. We estimated velocity and displacement waveforms from the original acceleration waveforms with a new parameter  $f'$  for correcting their baseline offsets and then compared the OBP record with these waveforms at each common site in both time and frequency domains. The OBP records agree with the acceleration waveforms in the frequency range of 0.05–0.15 Hz at almost all the stations. Based on this result, we proposed a new early tsunami detection scheme to extract most of tsunami and ocean-bottom displacement components from OBP records, including the coseismic period of large seafloor shakings.

The proposed extraction scheme enables us to estimate the tsunami component as well as the ocean bottom deformation at every 10 s only after 30 s of the origin time. As shown in Figure 10a, the waveforms estimated by this scheme show very good agreement with conventional 100-s low-pass filtered records which require their record length of more than 300 s. In other words, the proposed scheme can estimate tsunami and sea-bottom deformation signals from near-fault OBP records with high reliability much faster than any conventional methods.

Even if the assumptions of the proposed scheme cannot be simply applied to large earthquakes, this method may be rather robust or will not give fatally erratic tsunami sizes. This is because the last step of our method (Step 5), taking the average in each record segment of the 60 s time windowed record, works as a stable low-pass filter, suppressing the majority of sea bottom acceleration components. In fact, the result of application to the 2003 Tokachi-oki earthquake (section 5.3) shows good agreement even with the  $M_w$ 8.3 earthquake and the PGA about three times of the Off-Mie earthquake. The same may be true in the case of tsunami earthquakes, that is, if there are dominant acceleration components below 0.05 Hz, our method will give good results.

Several near-fault tsunami warning systems have been proposed in use of ocean-bottom records of tsunamis and sea bottom deformations (e.g., Inoue et al., 2019; Tanioka, 2018; Tsushima et al., 2012). Their practice will be soon tested to real-time cabled OBP data such as DONET and S-net. Under such a situation, our new scheme will assist them to be more rapid and reliable as a new powerful complimentary approach from a completely different point of view.

To apply our tsunami detection scheme to truly great megathrust earthquakes such as the Tohoku-oki earthquake of 2011 March 11, we will have to test our major assumption in this study, that is, an OBP gauge records sea-bottom accelerations in the frequency range of 0.05–0.15 Hz, regardless of the magnitude of ground shakings. While the relationship between the frequency range and PGA is almost constant in Figure 3d, we found some disagreements in waveforms at some stations, as shown in Figure 5. As shown in Figure 7, we concluded that strong horizontal shakings were recorded partly by vertical accelerometers. We will need examples of large events to investigate the origin of the disagreements found in this study because the number of stations was only 20 and the magnitude of the event was only  $M_w$ 6.0 as unavoidable lack of available data in the present.

Since the operation of DONET started in August 2011, but its coverage area is limited, there was a single event that occurred inside a network with the substantial amount of tsunamis at the stage of this study. On the other hand, S-net, a much larger array, has just started its operation, so there have been no tsunami data available in research yet. The  $M_w$ 7.4 Off-Fukushima earthquake of 2016 November 22, for example, occurred in the S-net area and generated over 50 cm tsunamis (Gusman et al., 2017). The records of such events larger than the one in this study will help us to check whether our assumption in this study will still be valid or not. The more we analyze the records of OBP gauges and seismometers for various types and sizes of earthquakes, the more our tsunami detection scheme will be improved. Such useful data will become abundant soon under the recent rapid development of ocean bottom networks.

## Data Availability Statement

The records of DONET strong-motion accelerometers were provided by the NIED website (doi: 10.17598/NIED.0008). The records of PG1 and OBS1 of the Tokachi-oki earthquake were provided by the Submarine Cable Data Center website of JAMSTEC ([https://www.jamstec.go.jp/scdc/top\\_e.html](https://www.jamstec.go.jp/scdc/top_e.html)).

## Acknowledgments

We thank NIED and JAMSTEC for providing the records of OBPG gauges and ocean-bottom seismometers used in this study. We would like to thank Narumi Takahashi for providing us with the DONET OBPG data prior to their official open release.

## References

- An, C., Cai, C., Zheng, Y., Meng, L., & Liu, P. (2017). Theoretical solution and applications of ocean bottom pressure induced by seismic seafloor motion. *Geophysical Research Letters*, *44*, 10,272–10,281. <https://doi.org/10.1002/2017GL075137>
- Boore, D. M. (2001). Effect of baseline corrections on displacements and response spectra for several recordings of the 1999 Chi-Chi, Taiwan, earthquake. *Bulletin of the Seismological Society of America*, *91*(5), 1199–1211. <https://doi.org/10.1785/0120000703>
- Gica, E., Spillane, M., & Titov, V. (2008). Development of the forecast propagation database for NOAA's Short-term Inundation Forecast for Tsunamis (SIFT) (NOAA Technical Memorandum OAR PMEL-139). Seattle, WA: Pacific Marine Environmental Laboratory.
- Gusman, A. R., Satake, K., Shinohara, M., Sakai, S., & Tanioka, Y. (2017). Fault slip distribution of the 2016 Fukushima earthquake estimated from tsunami waveforms. *Pure and Applied Geophysics*, *174*(8), 2925–2943. <https://doi.org/10.1007/s00024-017-1590-2>
- Hirata, K., Aoyagi, M., Mikada, H., Kawaguchi, K., Kaiho, Y., Iwase, R., et al. (2002). Real-time geophysical measurements on the deep seafloor using submarine cable in the southern kurile subduction zone. *IEEE Journal of Oceanic Engineering*, *27*(2), 170–181.
- Honda, R., Aoi, S., Morikawa, N., Sekiguchi, H., Kunugi, T., & Fujiwara, H. (2004). Ground motion and rupture process of the 2003 Tokachi-oki earthquake obtained from strong motion data of K-NET and KiK-net. *Earth Planets Space*, *56*(3), 317–322. <https://doi.org/10.1186/BF03353058>
- Inoue, M., Tanioka, Y., & Yamanaka, Y. (2019). Method for near-real time estimation of tsunami sources using ocean bottom pressure sensor network (S-net). *Geosciences*, *9*, 310. <https://doi.org/10.3390/geosciences9070310>
- Iwan, W. D., Moser, M. A., & Peng, C.-Y. (1985). Some observations on strong-motion earthquake measurement using a digital accelerometer. *Bulletin of the Seismological Society of America*, *75*(5), 1225–1246. <https://doi.org/10.1086/622062>
- Jamelot, A., & Raymond, D. (2015). New tsunami forecast tools for the French polynesia tsunami warning system part II: Numerical modelling and tsunami height estimation. *Pure and Applied Geophysics*, *172*(3), 805–819. <https://doi.org/10.1007/s00024-014-0997-2>
- Japan Agency for Marine-Earth Science and Technology (n.d.). Measurement instruments. <https://www.jamstec.go.jp/donet/e/rd/>
- Kanazawa, T., Shinohara, M., Sakai, S., Utada, H., Shiobara, H., Yamada, T., et al. (2016). S-net project, cabled observation network for earthquakes and tsunamis, SubOptic 2016, WE2B3.
- Kaneda, Y., Kawaguchi, K., Araki, E., Matsumoto, H., Nakamura, T., Kamiya, S., et al. (2015). Development and application of an advanced ocean floor network system for megathrust earthquakes and tsunamis. In P. Favali, L. Beranzoli, & A. De Santis (Eds.), *SEAFLOOR OBSERVATORIES: A New Vision of the Earth from the Abyss* (pp. 643–662). Berlin, Heidelberg: Springer.
- Kawaguchi, K., Kaneko, S., Nishida, T., & Komine, T. (2015). Construction of the DONET real-time seafloor observatory for earthquakes and tsunami monitoring. In P. Favali, L. Beranzoli, & A. De Santis (Eds.), *SEAFLOOR OBSERVATORIES: A New Vision of the Earth from the Abyss* (pp. 211–228), Springer Praxis Books. Berlin, Heidelberg: Springer.
- Kubo, H., Nakamura, T., Suzuki, W., Dhakal, Y. P., Kimura, T., Kunugi, T., et al. (2019). GroundMotion characteristics and nonlinear soil response observed by DONET1 seafloor observation network during the 2016 Southeast OffMie, Japan, Earthquake. *Bulletin of the Seismological Society of America*, *109*(3), 976–986. <https://doi.org/10.1785/0120170296>
- Kubo, H., Nakamura, T., Suzuki, W., Kimura, T., Kunugi, T., Takahashi, N., & Aoi, S. (2018). Site amplification characteristics at Nankai seafloor observation network, DONET1, Japan, evaluated using spectral inversion. *Bulletin of the Seismological Society of America*, *108*(3), 1210–1218. <https://doi.org/10.1785/0120170254>
- Kubota, T., Hino, R., Inazu, D., Ito, Y., Iinuma, T., Ohta, Y., et al. (2017). Coseismic slip model of offshore moderate interplate earthquakes on March 9, 2011 in Tohoku using tsunami waveforms. *Earth and Planetary Science Letters*, *458*, 241–251. <https://doi.org/10.1016/j.epsl.2016.10.047>
- Kubota, T., Suzuki, W., Nakamura, T., Chikazawa, N. Y., Aoi, S., Takahashi, N., & Hino, R. (2018). Tsunami source inversion using time-derivative waveform of offshore pressure records to reduce effects of non-tsunami components. *Geophysical Journal International*, *215*(2), 1200–1214. <https://doi.org/10.1093/GJI/GGY345>
- Maeda, T., Obara, K., Shinohara, M., Kanazawa, T., & Uehira, K. (2015). Successive estimation of a tsunami wavefield without earthquake source data: A data assimilation approach toward real-time tsunami forecasting. *Geophysical Research Letters*, *42*, 7923–7932. <https://doi.org/10.1002/2015GL065588>
- Mary, T. (2017). Metrozet TSA-100S accelerometer response. [https://ds.iris.edu/NRL/sensors/metrozet/metrozet\\_tsa100s\\_sensors.html](https://ds.iris.edu/NRL/sensors/metrozet/metrozet_tsa100s_sensors.html)
- Matsumoto, H., Araki, E., Kawaguchi, K., Nishida, S., & Kaneda, Y. (2013). Some characteristics of bottom pressure sensors of DONET. In *2013 IEEE International Underwater Technology Symposium (UT)* (pp. 1–7). <https://doi.org/10.1109/UT.2013.6519863>
- Matsumoto, H., Hayashi, Y., & Kaneda, Y. (2012). Characteristics of water pressure disturbances on real-time tsunami data of ocean-bottom pressure gauges. *Journal of Japan Society of Civil Engineers, Series B2 (Coastal Engineering)*, *68*(2), I\_391–I\_395. <https://doi.org/10.2208/kaigan.68.i391>
- Matsumoto, K., Takanezawa, T., & Ooe, M. (2000). Ocean tide models developed by assimilating TOPEX/POSEIDON altimeter data into hydrodynamical model: A global model and a regional model around Japan. *Journal of Oceanography*, *56*, 567–581.
- Mochizuki, M., Kanazawa, T., Uehira, K., Shimbo, T., Shiomi, K., Kunugi, T., et al. (2016). S-net project: Construction of large scale seafloor observatory network for tsunamis and earthquakes in Japan, AGU Fall Meeting, NH43B-1840. <http://adsabs.harvard.edu/abs/2016AGUFMNH43B1840M>
- National Research Institute for Earth Science and Disaster Resilience (2019). NIED DONET, National Research Institute for Earth Science and Disaster Resilience.
- Nosov, M., Karpov, V., Kolesov, S., Sementsov, K., Matsumoto, H., & Kaneda, Y. (2018). Relationship between pressure variations at the ocean bottom and the acceleration of its motion during a submarine earthquake. *Earth Planets Space*, *70*(1), 100.
- Saito, T. (2017). Tsunami generation: Validity and limitations of conventional theories. *Geophysical Journal International*, *210*, 1888–1900. <https://doi.org/10.1093/gji/ggx275>
- Saito, T., & Tsushima, H. (2016). Synthesizing ocean bottom pressure records including seismic wave and tsunami contributions: Toward realistic tests of monitoring systems. *Journal of Geophysical Research: Solid Earth*, *121*, 8175–8195. <https://doi.org/10.1002/2016JB013195>

- Tanioka, Y. (2018). Tsunami simulation method assimilating ocean bottom pressure data near a tsunami source region. *Pure and Applied Geophysics*, *175*(2), 721–729. <https://doi.org/10.1007/s00024-017-1697-5>
- Tanioka, Y., & Gusman, A. R. (2018). Near-field tsunami inundation forecast method assimilating ocean bottom pressure data: A synthetic test for the 2011 Tohoku-oki tsunami. *Physics of the Earth and Planetary Interiors*, *283*, 82–91. <https://doi.org/10.1016/j.pepi.2018.08.006>
- Tanioka, Y., Nishimura, Y., Hirakawa, K., Imamura, F., Abe, I., Abe, Y., et al. (2004). Tsunami run-up heights of the 2003 Tokachi-oki earthquake. *Earth Planets Space*, *56*(3), 359–365. <https://doi.org/10.1186/BF03353065>
- Tsushima, H., Hino, R., Tanioka, Y., Imamura, F., & Fujimoto, H. (2012). Tsunami waveform inversion incorporating permanent seafloor deformation and its application to tsunami forecasting. *Journal of Geophysical Research*, *117*, 1–20. <https://doi.org/10.1029/2011JB008877>
- Uehira, K., Kanazawa, T., Mochizuki, M., Fujimoto, H., Noguchi, S., Shinbo, T., et al. (2016). Outline of seafloor observation network for earthquakes and tsunamis along the Japan Trench (S-net), European Geosciences Union General Assembly 2016, EGU2016-13832.
- Wallace, L. M., Araki, E., Saffer, D., Wang, X., Roesner, A., Kopf, A., et al. (2016). Near-field observations of an offshore Mw 6.0 earthquake from an integrated seafloor and subseafloor monitoring network at the Nankai Trough, southwest Japan. *Journal of Geophysical Research: Solid Earth*, *121*, 8338–8351. <https://doi.org/10.1002/2016JB013417>
- Wang, D., Becker, N. C., Walsh, D., Fryer, G. J., Weinstein, S. A., McCreery, C. S., et al. (2012). Real-time forecasting of the April 11, 2012 Sumatra tsunami. *Geophysical Research Letters*, *39*, L19601. <https://doi.org/10.1029/2012GL053081>
- Wang, Y., Satake, K., Maeda, T., & Gusman, A. R. (2017). Green's function-based tsunami data assimilation: A fast data assimilation approach toward tsunami early warning. *Geophysical Research Letters*, *44*, 10,282–10,289. <https://doi.org/10.1002/2017GL075307>
- Wang, R., Schurr, B., Milkereit, C., Shao, Z., & Jin, M. (2011). An improved automatic scheme for empirical baseline correction of digital strong-motion records. *Bulletin of the Seismological Society of America*, *101*(5), 2029–2044. <https://doi.org/10.1785/0120110039>
- Wu, Y. M., & Wu, C. F. (2007). Approximate recovery of coseismic deformation from Taiwan strong-motion records. *Journal of Seismology*, *11*(2), 159–170. <https://doi.org/10.1007/s10950-006-9043-x>
- Yamamoto, N., Aoi, S., Hirata, K., Suzuki, W., Kunugi, T., & Nakamura, H. (2016). Multi-index method using offshore ocean-bottom pressure data for real-time tsunami forecast. *Earth Planets Space*, *68*(1), 128. <https://doi.org/10.1186/s40623-016-0500-7>
- Yamanaka, Y., & Kikuchi, M. (2003). Source process of the recurrent Tokachi-oki earthquake on September 26, 2003, inferred from teleseismic body waves. *Earth Planets Space*, *55*(12), e21–e24. <https://doi.org/10.1186/BF03352479>